RSC Advances

PAPER

View Article Online
View Journal | View Issue

Cite this: *RSC Adv.*, 2024, **14**, 18277

Adsorption and biodegradation of the azo dye methyl orange using *Ralstonia pickettii* immobilized in polyvinyl alcohol (PVA)–alginate–hectorite beads (BHec-RP)

Asranudin,[ab] Adi Setyo Purnomo,[*a] Holilah,[b] Didik Prasetyoko,[a] Noureddine El Messaoudi,[c] Alya Awinatul Rohmah,[a] Alvin Romadhoni Putra Hidayat[a] and Riki Subagyo[a]

Biological methods are widely used to treat dye waste, particularly methyl orange (MO) dye. The importance of MO degradation stems from its classification as a toxic dye. Within the scope of this research, successful bio-decolorization of MO was achieved through the use of *Ralstonia pickettii* bacteria immobilized in a PVA–alginate–hectorite matrix (BHec-RP). The optimum conditions for the degradation were observed at a composition of PVA (10%), hectorite (1%), static incubation, 40 °C, and pH 7. Subsequently, the adsorption kinetics of BHec-RP (dead cells) as well as the degradation kinetics of BHec-RP (live cells) and MO using free *R. pickettii* cells were evaluated. The decolorization of MO using BHec-RP (dead cells) is an adsorption process following pseudo-first-order kinetics (0.6918 mg g^{-1} beads) and occurs in a monolayer or physical process. Meanwhile, the adoption of BHec-RP (live cells) and free *R. pickettii* cells shows a degradation process under pseudo-first-order kinetics, with the highest rates at an initial MO concentration of 50 mg L^{-1} being 0.025 mg L^{-1} h^{-1} and 0.015 mg L^{-1} h^{-1}, respectively. These results show that the immobilization system is superior compared to free *R. pickettii* cells. Furthermore, the degradation process shows the inclusion of several enzymes, such as azoreductase, NADH-DCIP reductase, and laccase, presumed to be included in the fragmentation of molecules. This results in five fragments based on LC-QTOF/MS analysis, with *m*/*z* values of 267.12; 189.09; 179.07; 169.09; and 165.05.

Received 20th December 2023
Accepted 10th May 2024

DOI: 10.1039/d3ra08692e

rsc.li/rsc-advances

Introduction

The global production of synthetic dyes is estimated to reach 7 × 10^5 tons per year for nine groups of dyes, namely acid, basic, mordant, sulfur, dispersion, reactive, direct, vat, and azo dyes.[1] Among these dyes, azo dyes (R′–N=N–R″) constitute the dominant group, representing approximately 70% of the total colorants.[2,3] Synthetic dyes are used in various industrial sectors, including textiles, pharmaceuticals, printing, paper, food, leather, and laboratories, as indicators and stains for biological specimens.[4–6] The extensive use of synthetic dyes is consistent with the ease of water contamination. This influences the increase in chemical oxygen demand (COD), biochemical oxygen demand (BOD), as well as dissolved and suspended solids. Under anaerobic conditions, microorganisms can metabolize dyes, producing toxic intermediate products.[7] Methyl orange (MO) is an azo dye identified to produce intermediate products such as aromatic amines, including *N*,*N*-dimethyl benzyl-1,4-diamine, sulfonamide, and 1,4-diaminobenzene.[8,9] These products are reported to be highly toxic due to their transformation into mutagenic, carcinogenic, and teratogenic species.[8,10–12] Additionally, synthetic dyes have the potential to induce damage to the vital organs of humans and animals, including the kidneys, digestive system, brain, liver, skin, and central nervous system.[1,13,14]

Various methods, such as flocculation, adsorption, coagulation, sedimentation, ultrafiltration, electrolysis, ion exchange, and plasma, have been used to eliminate dye from solutions.[15–20] However, the complete decolorization of dye has not been achieved due to its intricate molecular composition and the presence of toxic byproducts.[21,22] Many microorganisms, including bacteria,[23] fungi,[24] and yeast,[25] have shown their ability to remove the color from azo dyes through bioabsorption,[26] degradation,[27] and mineralization.[28] Among these microorganisms, bacteria have been proven to play a crucial role in the treatment of wastewater containing dyes.[13,29–31] Extensive research has shown the ability to effectively remove dyes. However, the use of free cells in the biodegradation

[a]*Department of Chemistry, Institut Teknologi Sepuluh Nopember (ITS), Surabaya, Indonesia. E-mail: adi_setyo@chem.its.ac.id*

[b]*Research Center or Biomass and Bioproducts, National Research and Innovation Agency of Indonesia (BRIN), Cibinong, 16911, Indonesia*

[c]*Laboratory of Applied Chemistry and Environment, Faculty of Sciences, Ibn Zohr University, Agadir 80000, Morocco*

process is limited by reaction rates, operational instability, dye toxicity, and inefficiency in transferring substrates.[32] To address these issues, immobilized cells have been developed as an appropriate method in the field of biodegradation. These cells tend to show high enzymatic activity and greater resistance to various environmental disturbances, such as changes in pH, high concentrations, and inhibitory ions.[12,33] Additionally, immobilized cells are more advantageous regarding oxygen supply, mass transfer, and repeated use.[12,34]

A PVA–alginate mixture is the main supporting material for cell immobilization, widely applied.[35–38] This is preferred because the mixture can form perfectly round beads, possess strong mechanical characteristics, and stabilize cells. However, the polymer results in a denser surface for the beads, limiting mass transfer within the system. Some studies found that adding a small amount of alginate to the PVA gel-making process improved the tissue structure and enhanced the mass transfer of the carrier.[39,40] However, the polymer mixtures still show high density, influencing cell viability and pollutant degradation rates.[41] This limitation can be addressed by adding adsorbents such as kaolin clay,[32,36] bentonite,[37] and diatomaceous earth[40] into the PVA–alginate gel. Lin *et al.*[41] reported that adsorbents enhanced the mechanical properties of the gel, providing pores and acting as an adhesive medium that enhanced microbial stability.[1,40,41] A potential adsorbent is hectorite, which has a structure and composition similar to those of bentonite and kaolin. This adsorbent shows biocompatibility in the PVA–alginate mixture, is non-toxic, hydrophilic, and provides large pores.[2,3,42] Therefore, hectorite can be used as the base material for bacterial cell immobilization to enhance the rate of pollutant degradation.

The bacteria immobilized on PVA–alginate–hectorite is *Ralstonia pickettii*. This is the first report of *R. pickettii* immobilization for MO degradation. The ability to degrade dyes and other toxic pollutants such as methylene blue,[43] DDT (1,1,1-trichloro-2,2-bis(4-chlorophenyl)ethane)[44–46] and crude oil[47] has been stated. The degradation of MO as a model pollutant was evaluated under various parameters, such as PVA content, hectorite content, pH, and temperature. The immobilization carrier material enhances the adsorption and degradation rates. Additionally, the physical characterization of the beads, the enzymes, and the prediction of the MO degradation pathway were reported.

Experimental

Materials

The stock culture of *R. pickettii* NBRC 102503 was purchased from NITE Biological Resource Center (NBRC), Chiba, Japan, LiCl (Merck, Germany), $Mg(OH)_2$ (Merck, Germany), ludox HS40 (Sigma-Aldrich, Germany), cetyltrimethylammonium bromide (CTABr), (Merck, Germany), MO (C.I. 13025), (Merck, Germany), $CaCl_2 \cdot 2H_2O$ (SAP, Indonesia), polyvinil alcohol (PVA; Mw. approx. 60 000; Merck, Germany), alginate (HiMedia, India), Luria-Bertani broth (Merck, Germany), Nutrient agar (HiMedia, India), bovine serum albumin (Merck, Germany), 2,2-azino-bis(3-ethylbenzothiazoline-6-sulfonic acid) (ABTS), 2,6-dichlorophenolindophenol (DCIP) (Merck, Germany). Furthermore, mineral salts medium (g L^{-1}): K_2HPO_4 (1,73), KH_2PO_4 (0.68), $MgSO_4 \cdot 7H_2O$ (0,1), NaCl (0,1), $FeSO_4 \cdot 7H_2O$ (0,03), NH_4NO_3 (1), $CaCl_2 \cdot 2H_2O$ (0.2), and $C_6H_{12}O_6$ (1) were of analytical grade.

Regeneration and production of *R. pickettii* for immobilization

Bacterium culture *R. pickettii* NBRC 102503 was maintained on nutrient agar and incubated at 37 °C for 24 hours. The colony was inoculated into 10 mL of LB broth in an Erlenmeyer flask, and the cultures were pre-incubated at 37 °C for 30 hours with a shaker of 120 rpm. In addition, the inoculum size was fixed to optical density 1.0 (λ_{max} = 600 nm, 1.50 × 10^6 cells per mL).

Synthesis of hectorite

Hectorite-CTAB was synthesized using the method described by Asranudin.[2,3] In this synthesis, 40% CTAB was added to the $LiCl : Mg(OH)_2 : SiO_2$ (1.33 : 5.00 : 7.60), and the resulting mixture was subjected to calcination at 550 °C in a nitrogen environment for 1 hour. This was followed by exposure to air for 4 hours, and the calcined hectorite was mixed with PVA hydrogel, sodium alginate (SA), and *R. pickettii* cells.

Batch experiments and analysis methods

Factors influencing the biodegradation of MO in BHec-RP were investigated. Experiments were conducted using various concentrations of PVA, namely 2.5%, 5.0%, 7.5%, 10%, and 15% (w/v), as well as hectorite, including 0.5%, 1%, 2%, 3%, and 4% (w/v). This mixture contained 1% (w/v) alginate, and the *R. pickettii* pellets were regenerated to an optical density of 1.0 (λ_{max} = 600 nm, 1.50 × 10^6 cells per mL). The experiments were performed in triplicate and incubated in a stationary incubator under dark conditions. MO concentration was monitored for up to 48 hours, and the PVA–alginate–hectorite–RP hydrogel was dropped into a mixture of H_3BO_3 solution (3% b/v) and $CaCl_2$ (4% b/v) using aseptic syringes. The mixture was stored for 12 hours to obtain hardened gel beads with a diameter of approximately 3–5 mm. The beads were washed three times with demineralized water to remove residual $CaCl_2$ and stored

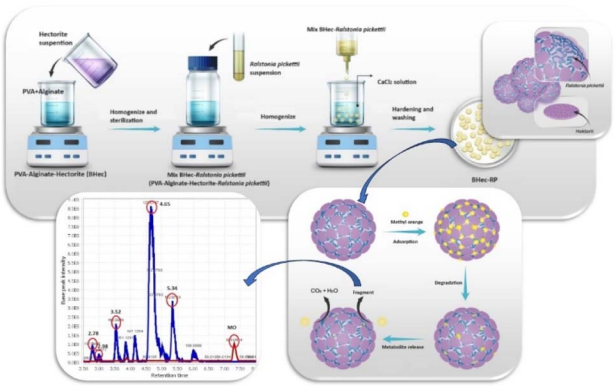

Fig. 1 Illustrative of preparation methodology for BHec-RP.

in a 0.5% NaCl solution at 4 °C for long-term use. The obtained beads are denoted BHec-RP, and an illustration of the fabrication is shown in Fig. 1.

Adsorption and degradation kinetics of methyl orange (MO)

The adsorption and degradation kinetics were determined using dead and live cells in BHec-RP. The reactions were carried out in 100 mL Erlenmeyer flasks containing 2.5 g of beads and 25 mL of MSM solution, with a final MO concentration ranging from 50 to 300 mg L^{-1}. The decolorization was performed at 40 °C under static conditions. Furthermore, the degradation kinetics using free *R. pickettii* cells were also studied for comparison. The residual MO concentration was determined using UV-vis spectrophotometry at a wavelength of 465 nm based on eqn (1).

$$\%\ \text{Degradation} = \frac{C_0 - C_t}{C_0} \times 100 \quad (1)$$

Meanwhile, the adsorption capacity of BHec-RP (dead cell) was determined using eqn (2).

$$q = \frac{C_0 - C_t}{m} \times V \quad (2)$$

where C_0 is the initial concentration of the dye (mg L^{-1}); C_t is the dye concentration (mg L^{-1}) at time t (h) for beads containing dead cells; m is the mass of the beads in the experiment; and V is the volume of the reaction solution in the system. The kinetics of MO degradation by free cells and BHec-RP (live cells) were determined using the first-order kinetics equation. In addition, the reusability and stability tests of BHec-RP (live cells) against MO were conducted for a total of 8 cycles and stored for 50 days.

Enzyme analysis and identification of metabolite products

Crude enzyme extract was obtained by centrifuging the decolorization media at 4000 rpm at 4 °C for 10 minutes. The obtained filtrate was tested for enzyme activity and adopted for total protein analysis using the Bradford method.[48] The enzymes analyzed were NADH-DCIP reductase,[49] azoreductase,[50] and laccase.[51]

The identification of metabolites after decolorization was determined using Q-TOF LC/MS (Bruker). A 50 mL aliquot of the cell culture medium was centrifuged at 4000 rpm for 15 minutes, and the collected supernatant was extracted with ethyl acetate. The extract was dried using a rotary vacuum evaporator and re-dissolved in ethanol for further analysis. The elution method used a gradient of 0.2 mL min^{-1} for the first three minutes and 0.4 mL min^{-1} for the subsequent seven minutes. The mobile phase used was methanol and water, with a ratio of 99 : 1 (v/v) for the first 3 minutes and 61 : 39 (v/v) for the following seven minutes. This analysis used an Acclaim TM RSLC 120 C18 column (2.1 × 100 mm) at a temperature of 33 °C. Various tools, including ChemDraw Ultra 12, MZmine3, and PathPred (**https://www.genome.jp/tools/pathpred/**), were used to determine the logic of metabolite fragments.

Characterization

Beads BHec-RP before and after application have been characterized using relevant instruments. Morphological analysis and elemental composition were determined using SEM-EDX (Hitachi, FlexSEM 1000). Before characterization, BHec-RP was freeze-dried at −50 °C for 8 hours. Thermal analysis of BHec-RP was performed using TGA/DTG (Hitachi High-Tech Sciences STA7200 Simultaneous Thermal). The sample was heated from 28 to 900 °C at a rate of 10 °C min^{-1} under a 60 mL min^{-1} nitrogen stream. In addition, the surface and pore area of BHec-RP were analyzed through the Quantachrome Touchwin v1.11 instrument. The sample was degassed at 300 °C for 3 hours under a vacuum, and N_2 gas flowed at −196 °C. The specific surface area and the pore size distribution were calculated using BET (Brunauer–Emmet–Teller) and DFT (Density Functional Theory).

Results and discussion

Characterization

Scanning electron microscope. SEM images of BHec (No Cell), BHec-RP, Hec-40, and TEM of Hec-40 are shown in Fig. 2. Dry BHec and BHec-ARP beads have a diameter of ∼5 mm, as shown in Fig. 2a and b. The enlarged part of the beads on the right shows that the surface morphology of hectorite beads differs from the powder form due to the intercalation of PVA and alginate.[52] BHec and BHec-RP report the presence of a network confirming the encapsulation of hectorite in alginate. Asranudin *et al.*[3] stated that the successful intercalation of hectorite in alginate resulted in a network-like morphology of its beads. The morphological difference between BHec and BHec-RP is the presence of *R. pickettii* on BHec-RP, appearing as round shapes attached to the network. Hec-40, the morphology of hectorite containing 40% CTAB before calcination, shows

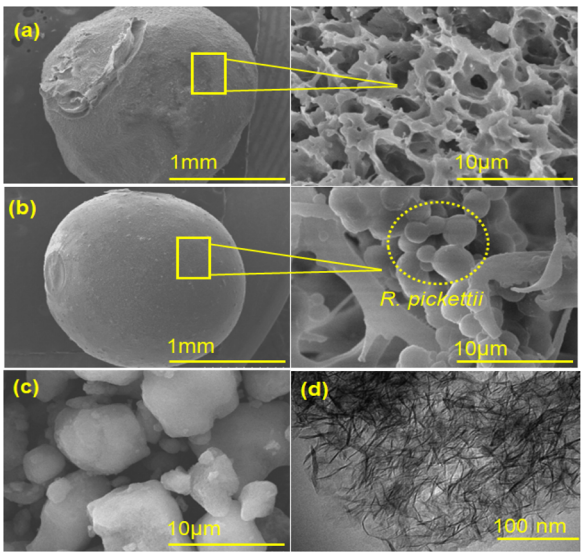

Fig. 2 Micrographs: (a) SEM of BHec, (b) SEM of BHec-RP, (c) SEM of Hec-40, and (d) TEM of Hec-40 (after calcination).

Table 1 Element Content in BHec, BHec-RP, and Hec-40

	% Weight		
Elements	BHec	BHec-RP	Hec-40
C	4.84	10.27	—
N	—	4.10	—
O	44.92	57.25	52.34
Mg	0.99	2.14	14.48
Si	1.85	3.62	29.81
Cl	23.35	2.92	3.38
Ca	22.72	17.66	—
Na	1.33	2.04	—

irregularities (Fig. 2c). Fig. 2d reports the morphology of Hec-40 after calcination, showing a silicate layer characteristic.[53] Furthermore, elemental analysis of BHec, BHec-RP, and Hec-40 is presented in Table 1. The difference in composition between these two beads is that BHec does not contain the element N. The presence of N in BHec-RP beads is due to *R. pickettii*. Additionally, the weighted C value increases significantly with the presence of bacteria in the beads, reaching 10.27%. Hec-40 does not contain C and N since these elements are lost during calcination.

The analysis of the morphology of BHec-RP beads before and after decolorization and BHec-RP (dead cells) after adsorption as control beads is shown in Fig. 3. Furthermore, the elemental analysis of BHec-RP is presented in Table 2. The interaction between MO and BHec-RP is confirmed through SEM images and elemental mapping using EDS, as presented in Fig. 3. These results depict the morphology of beads before (Fig. 3a) and after (Fig. 3b) application and those containing dead cells (Fig. 3c). The characterization shows that the PVA–alginate–hectorite mixture used as a supporting material allows effective trapping of *R. pickettii* cells, preventing any suspension detected in the decolorization media. Furthermore, live cells are visible in the beads in Fig. 3a and b, forming hanging spheres. This characteristic of *R. pickettii* is similar to that of *E. aerogenes* NBO2 and *L. plantarum* CM53, which form in the tissue of alginate beads.[54,55] The condition shows that the cells are protected and well-trapped in the supporting matrix. The composition of the immobilization carrier material can preserve cells and enzymes

Table 2 Elemental content in BHec-RP

	% Weight		
Elements	BHec-RP (before)	BHec-RP (after)	BHec-RP (dead cell and after)
C	10.27	19.79	18.58
N	4.10	4.51	4.03
O	57.25	61.58	46.27
Mg	2.14	0.46	0.40
Si	3.62	0.87	1.12
Cl	2.92	6.28	12.03
Ca	17.66	3.0	9.43
S	—	1.05	6.28
Na	2.04	2.47	5.28

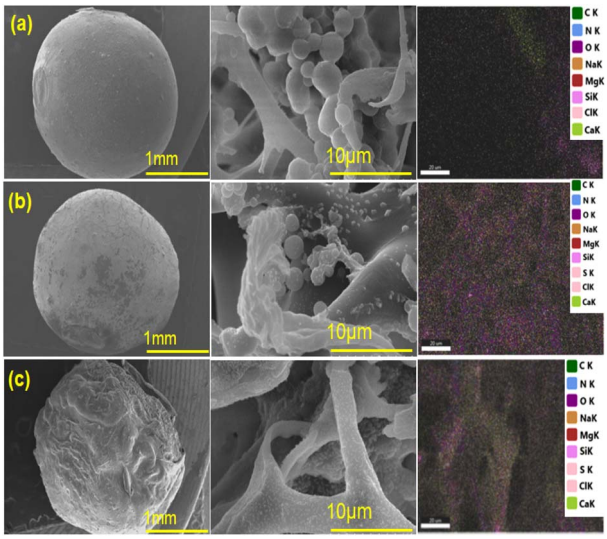

Fig. 3 SEM and EDS images: (a) BHec-RP (before); (b) BHec-RP (after); (c) BHec-RP (dead cell).

from environmental changes and denaturation. Furthermore, EDS analysis shows differences in the elemental composition between Fig. 3b and c. The sulfur content in Fig. 3b is lower than in Fig. 3c, showing MO adsorption. In comparison, in Fig. 3b, the content is presumed to be desulfonated by bacterial activity. The carbon is also higher in Fig. 3b and c, 19.79% and 18.58%, due to the adsorbed MO molecules on the beads' surface.

Thermal analysis

The thermal stability of the hectorite calcined sample (Hec), BHec (PVA–alginate–hectorite), and BHec-RP (PVA–alginate–hectorite-*R. pickettii*) was analyzed using TGA/DTG, as shown in Fig. 4. The thermogravimetric calcined hectorite (Hec) analysis showed a typical weight loss in two decomposition stages.[56] The first weight loss appeared at temperatures below 200 °C, associated with the dehydration of physically absorbed water on the surface of hectorite.[57] In this context, hectorite is a hydrophilic material with a high tendency to absorb water within its layers and surface. The second decomposition stage at ~731 °C is related to the dehydroxylation within the structure.[58] The DTG peak for the Hec-calcined sample was observed at the same temperature. Moreover, BHec and BHec-RP beads showed different decomposition stages. The first decomposition was shown below 200 °C, as well as at ~290 °C and ~430 °C. The decomposition at ~250 °C and ~430 °C shows that the degradation of PVA and alginate polymers occurs in multiple stages between 200–400 °C and 500–650 °C. This data suggests that BHec remains stable at high temperatures, allowing for mechanical stability.

Adsorption–desorption of N_2

This analysis compares the surface area and pores before and after immobilization in the PVA–alginate matrix. The N_2 adsorption–desorption curves of Hec and BHec-RP are shown in Fig. 5. This analysis compares the pore characteristics of Hec

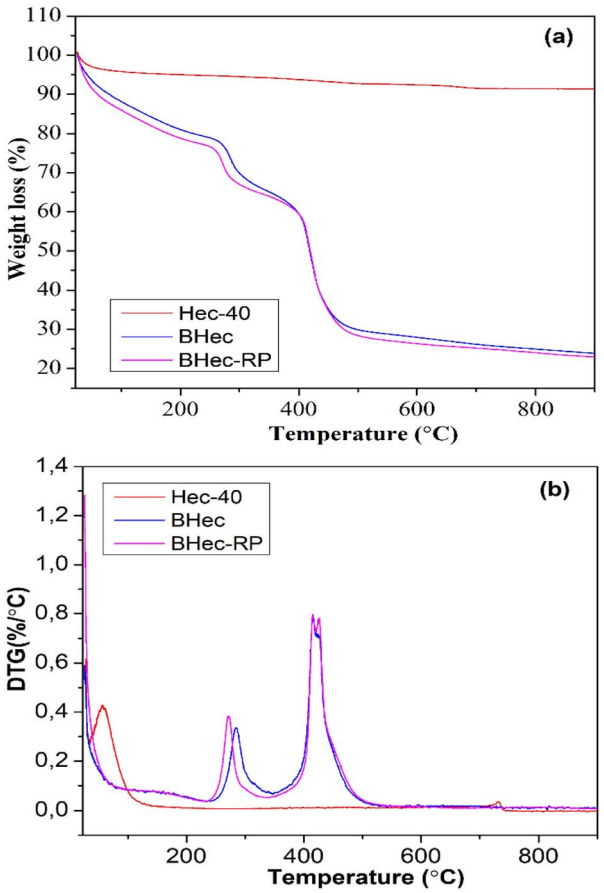

Fig. 4 TGA (a) and DTG (b) curves of Hec, BHec, and BHec-RP.

powder and its immobilized form. Hec serves as a source of pores that enhance mass transport into and out of BHec. Furthermore, Hec and BHec-RP samples show hysteresis loops in the range of 0.50–0.90 (P/P_0), consistent with the characteristics of Type IV isotherms and mesoporous materials. The bead samples show smaller hysteresis loops with lower V_{adsop} values.

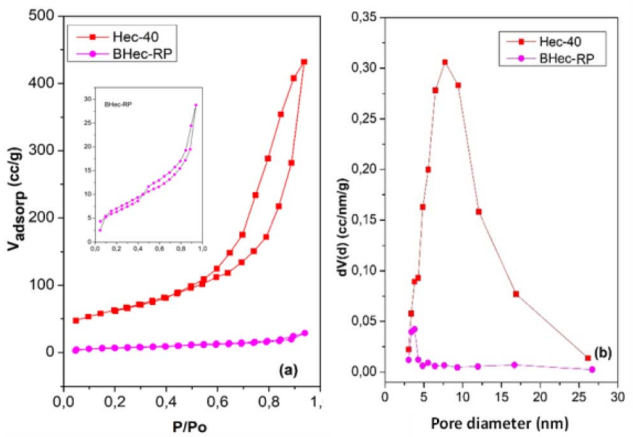

Fig. 5 N_2 adsorption–desorption (a) and PSD (b) curves of Hec and BHec-RP.

The surface area (S_{BET}) and S_{meso} of BHec-RP beads are lower than Hec, attributed to the intercalation of PVA and alginate species occupying the interlayer surface of hectorite.[42] According to the NLDFT method, the S_{BET} and S_{meso} for Hec and BHec-RP samples are 224.21 $m^2\ g^{-1}$, 22.40 $m^2\ g^{-1}$, and 217.45 $m^2\ g^{-1}$, 20.31 $m^2\ g^{-1}$, respectively. The pore diameter of BHec-RP is smaller than that of Hec, measuring 3.82 nm and 7.75 nm, respectively. This data shows that hectorite contributes to the pores and surface area in BHec-RP. The surface of area, pore diameter, and volume of Hec and BHec-RP samples are summarized in Table 3.

MO degradation using immobilized and free cells

The comparison of MO degradation using immobilized, sterilized immobilized, and free cells is shown in Fig. 6. The highest efficiency is achieved by BHec-RP and free cells after 30 and 48 hours of degradation, respectively. Therefore, *R. pickettii* cells can effectively degrade MO in immobilized and suspended states. The role of bacteria is evident when compared to BHec-RP beads (dead cells), which only achieved a decolorization of 24%, and the decolorization is an adsorption process. Rapid equilibrium is reached at 12 hours, showing that MO is adsorbed on the surface of the beads. In contrast, BHec-RP (live cells) and free *R. pickettii* show equilibrium after complete decolorization at 30 and 48 hours. BHec-RP (live cells) quickly reaches equilibrium because MO has been adsorbed since the early stages of interaction. Based on the decolorization profile, the adsorption and degradation processes occur simultaneously, resulting in a shorter time. In free *R. pickettii*, from 2 to 12 hours, only less than 30% is decolorized. Dye degradation using free cells is slow in the first 12 hours, and the cells are in an adaptation phase. Therefore, it is insufficient to adsorb and produce enzymes optimally. The toxicity of pollutants may lead to the cells adapting over time.[36,41,59,60] Similar conditions were reported in the decolorization of crystal violet using free cells of *Burkholderia vietnamiensis* C09V, where immobilized cells decolorized faster.[32]

Adsorption kinetics and MO degradation

In Fig. 6, the removal of methyl orange using immobilized cells resulted from MO first adsorbing onto beads and then degradation by the immobilized cells. Hence, adsorption (dead cells) and biodegradation kinetics (live cells) are investigated in this section to further confirm the mechanism.

Adsorption kinetics

Influence of contact time and initial concentration. The adsorption kinetics and degradation of MO were investigated in this section to confirm the occurring mechanism at 40 °C, pH 7, a volume of 25 mL, and 2.5 g of beads. Contact time and initial concentration on adsorption into BHec-RP (dead cells) are shown in Fig. 7. This subsection discusses the mechanism of MO adsorption into BHec-RP (dead cells). To understand the mechanism from aqueous solution into the BHec-RP (dead cells) matrix, the Lagergren kinetics model is used to research the pseudo-first-order and pseudo-second-order models in

Table 3 Surface area, pore diameter, and pore volume of Hec and BHec-RP samples

Sample	S_{BET} ($m^2\ g^{-1}$)	S_{meso} ($m^2\ g^{-1}$)	Pore diameter (nm)	Pore volume ($cm^3\ nm^{-1}\ g^{-1}$)
Hec-40	224.21	217.45	7.75	0.62
BHec-RP	22.40	20.31	3.82	0.04

a non-linear form.[37,41,61] The pseudo-first-order kinetics model can be described by eqn (3) and (4).

$$\frac{dq}{dt} = K_1(q_e - q) \quad (3)$$

Eqn (3) can be expanded as follows:

$$\ln(q_e - q) = \ln(q_e) - K_1 t \quad (4)$$

While the pseudo-second-order kinetics model is determined based on eqn (5) and (6):

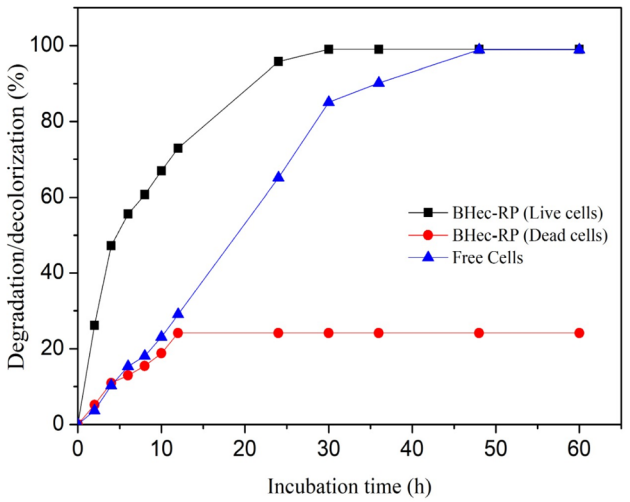

Fig. 6 Decolorization MO using BHec-RP (live and dead cells) and free cells (100 mg L^{-1}, static, pH 7, temperature 40 °C).

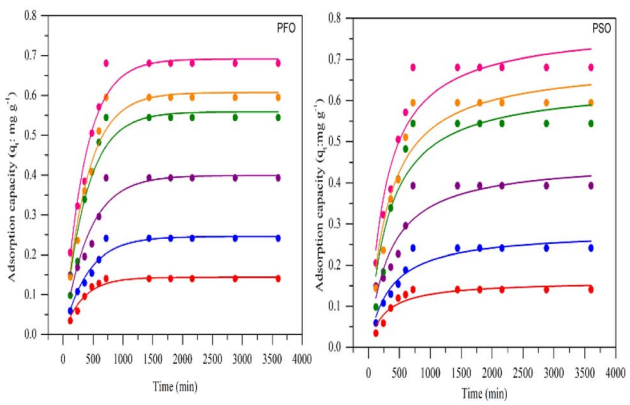

Fig. 7 MO adsorption capacity at different initial concentrations (PVA: 10% (w/w); alginate: 1% (w/w); hectorite: 1% (w/w); bead mass 10%, volume 25 mL).

$$\frac{dq}{dt} = K_2(q_e - q)^2 \quad (5)$$

Integration of eqn (5) yields:

$$\frac{t}{q} = \frac{t}{q_e} + \frac{1}{K_2 q_e^2} \quad (6)$$

where q_e is mg MO adsorbed per g BHec-RP (dead cells); q is the absorbed MO amount per gram of dead BHec-RP; K_1 is the first-order kinetic constant (1/min); and K_2 is the second-order kinetic constant ($g_{BHec\text{-}RP}\ mg_{MO}^{-1}\ min^{-1}$).

Fig. 7 shows the pseudo-first-order and pseudo-second-order non-linear plots of MO adsorption using initial concentrations of 50–300 mg L^{-1} at 40 °C. The results reported that equilibrium was reached after 12 hours of incubation, with a maximum adsorption capacity ranging from 0.14 to 0.68 mg g^{-1}. The initial MO concentration is a driving force to overcome mass transfer limitations between the absorbent and liquid phases. A high initial MO concentration enhances the driving force of mass transfer to increase adsorption capacity.[37] The first- and second-order kinetic analysis results are summarized in Table 4, showing the rate constant data (K_1 and K_2) as well as correlation coefficient values (R^2) for both models. Data in Table 4 show that the adsorption of MO into BHec-RP (dead cells) fits the pseudo-first-order kinetic model. The coefficient (R_1^2) for the pseudo-first-order model is higher than the pseudo-second-order model. Furthermore, the theoretical q_e values are also closer to the experimental results for all initial MO concentrations. This result shows that the pseudo-first-order model more accurately predicts MO adsorption on BHec-RP than the pseudo-second-order model.

Further analysis includes a nonlinear isotherm, and eqn (7) and (8) are used to determine the Langmuir and Freundlich nonlinear isotherm models:[62–64]

$$q_e = \frac{q_m K_L C_e}{1 + K_L C_e} \quad (7)$$

$$q_e = K_F C_e^{\frac{1}{n}} \quad (8)$$

where K_L (L mg^{-1}) and K_F (mg g^{-1}) are the Langmuir and Freundlich isotherm constants, respectively. Meanwhile, q_m represents the maximum Langmuir adsorption capacity, q_e is the adsorption capacity (mg g^{-1}), and C_e is the equilibrium concentration (mg L^{-1}) of MO. In this context, n is the dimensionless constant showing the affinity of MO adsorption to the adsorbent. Further analysis includes isotherms through the relationship between the initial concentration and the adsorption capacity of the beads, resulting in Langmuir and

Table 4 Kinetics parameters of pseudo-first- and pseudo-second-order models

		Pseudo-first-order			Pseudo-second-order		
Initial conc.	q_e (mg g^{-1})	q_{e1}	K_1/min	R_1^2	q_{e2}	K_2, g mg^{-1} min^{-1}	R_2^2
50	0.140366	0.1435	0.0031	0.945	0.1615	0.0245	0.862
100	0.241037	0.2457	0.0024	0.952	0.2822	0.0105	0.906
150	0.392927	0.3994	0.0024	0.948	0.4561	0.0065	0.867
200	0.544146	0.5587	0.0026	0.932	0.6419	0.0048	0.861
250	0.594817	0.6076	0.0026	0.955	0.6939	0.0046	0.895
300	0.680854	0.6918	0.0028	0.962	0.7805	0.0046	0.909

Freundlich sorption plots, as explained in Fig. 8. This adsorption process was carried out at 40 °C, with initial MO concentrations ranging from 50 to 300 mg L^{-1}. A summary of the evaluation of the models for the beads is presented in Table 5.

Fig. 8 shows that the Langmuir isotherm plot is more consistent with the data than the Freundlich isotherm. This is reflected in the summary of the analysis, which shows correlation coefficients (R^2) close to 1, while for the Freundlich isotherm, it is negative. Additionally, the sum of squared residuals (RSS) and reduced chi-square (Red. Chi-Sqr) values for the Langmuir isotherm are the smallest, showing a strong correlation. The conformity suggests that the adsorption of MO into the beads is a monolayer process with a maximum capacity of 2.374 mg g^{-1}.

Degradation kinetics

Several models have been applied to describe the biodegradation of organic pollutants. Exponential functions (pseudo-first-order kinetics) depict such biodegradation.[32,37,41] Therefore, this research determined the biodegradation kinetics of MO with BHec-RP (live cells) and free cells using the first-order equation based on Fig. 9a and b data using eqn (9). The rate constant can be calculated from the slope.

$$-\ln\frac{C}{C_0} = kt \quad (9)$$

where C_0 is the initial concentration of MO (mg L^{-1}), C is the concentration of MO (mg L^{-1}) at time t (hours), and k is the first-order rate constant for the biodegradation of MO (1/hour). Furthermore, the half-life of MO degradation can be obtained using eqn (10).

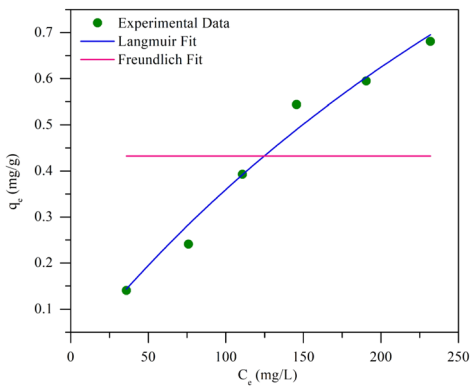

Fig. 8 Non-linear sorption isotherm on BHec-RP (dead cells).

$$t_{1/2} = \frac{\ln 2}{k} \quad (10)$$

The adoption of immobilized cells to degrade MO was investigated through various initial concentrations. The results are shown in Fig. 9a, where MO is significantly degraded by BHec-RP (live cells). Table 6 summarizes the data for the kinetics of MO degradation through BHec-RP (live cells), expressed by the first-order reaction model (R^2 > 0.90). The biodegradation rate constant k is directly proportional to the initial concentration of MO, with the rate constant ranging from 0.025 to 0.0017 mg L^{-1} h^{-1} at 50–150 mg L^{-1}, and concentrations above the value show a gradual decrease in the rate.

Similarly, as listed in Table 6, it also reports data on the kinetics of MO degradation by free *R. pickettii* cells, with the maximum rate being 0.015–0.014 mg L^{-1} h^{-1} at 50–100 mg L^{-1} MO, and concentrations >100 mg L^{-1} showing a decrease in the constant. These results show that higher MO concentrations reduce the biodegradation activity of BHec-RP and free *R. pickettii*. Based on the constant biodegradation rate k and half-time $t_{1/2}$, MO degradation by BHec-RP (live cells) is higher and faster than free *R. pickettii* cells. Zhang *et al.*[40] reported that immobilized cells are always superior. These results were consistent with other studies that used immobilized cells for the biodegradation of methyl violet,[65] ammonia,[40] fenol,[36] naftalen,[37] and azo dyes (Malachite green, Auramine yellow, MO).[66]

Factors affecting the biodegradation of methyl orange

Effect of PVA and hectorite concentration. The immobilization of *R. pickettii* into the matrix of polyvinyl alcohol, alginate, and hectorite was successfully conducted and applied to the degradation process of MO. The mixture of PVA–alginate–

Table 5 Non-linear sorption isotherm analysis of MO using BHec-RP (dead cells)

		Error		
Isotherm	Value	R^2	RSS	Red. Chi-sqr
Langmuir				
q_{max}	2.37398	0.97201	0.00502	0.00125
K_L	0.00179			
Freundlich				
K_F	0.43236	−0.25	0.22406	0.05601
n	-1.003×10^{23}			

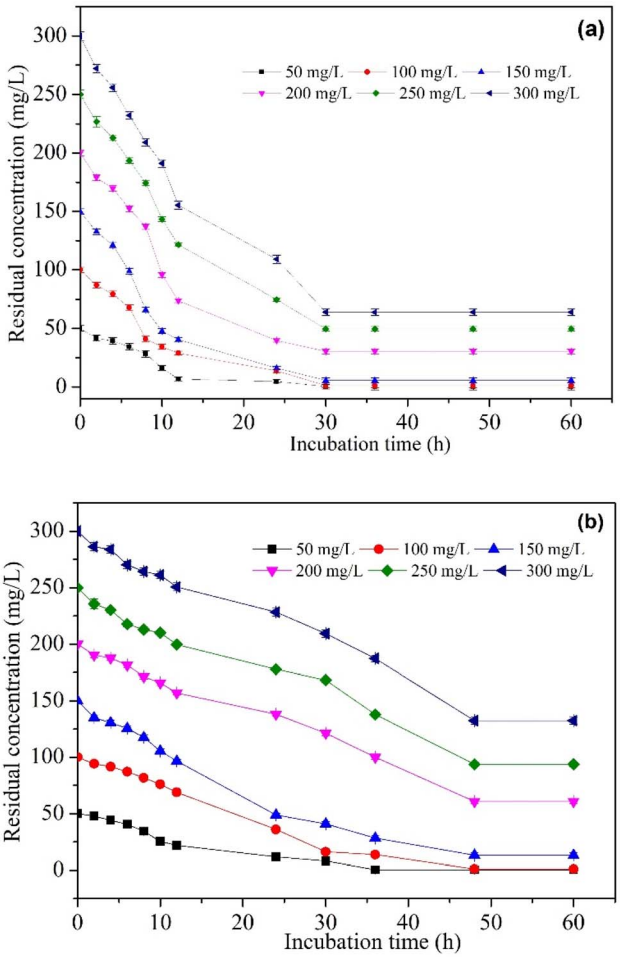

Fig. 9 The influence of initial MO concentrations on (a) BHec-RP (Live cells) and (b) Free *R. pickettii* cells.

hectorite–*R. pickettii* was abbreviated as BHec-RP. This research performed variations in PVA (2.5–15%) and hectorite levels (0.5–4%), as shown in Fig. 10. The alginate level was 1%, and the inoculum was adjusted to the mixture volume at a bacterial density of OD 600 = 1 absorbance. Zhang *et al.*[40] reported that alginate content exceeding 1% led to denser bead structures and influenced a decrease in cell viability due to the limited bacterial adhesion space.

Fig. 10 shows that the optimal levels of immobilization carriers for *R. pickettii* are PVA 10% (w/v) and hectorite 1% (w/v).

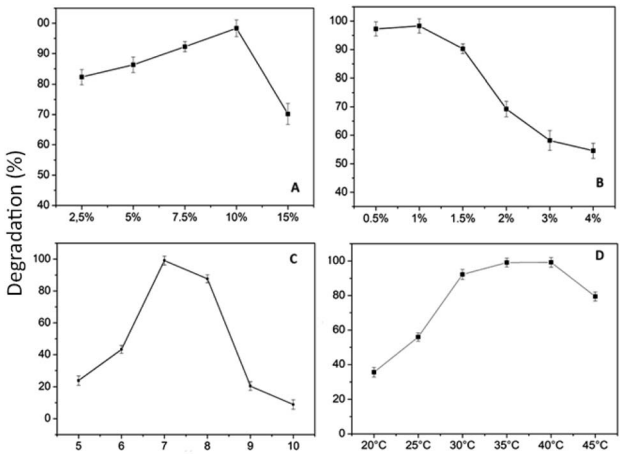

Fig. 10 Effect of: (a) PVA concentration; (b) hectorite concentration; (c) pH; (d) temperature.

In Fig. 10a, the matrix's PVA concentration significantly affects the MO degradation rate. The appropriate PVA content determines the mechanical properties of BHec-RP beads. This research found that 2.5–7.5% PVA levels showed a perfect round shape but low mechanical properties, as shown by breakage when pressed with fingers. A PVA concentration of 10% showed high mechanical stability, resisting breakage when pressed and producing perfectly round beads (Fig. 11). In contrast, a PVA concentration of 15% resulted in very rigid or hard beads. A PVA concentration of 10% showed optimum mechanical properties and a degradation rate.[36,37,40,65] El-Naas *et al.*[67] reported that a PVA content of 10% produces high porosity and a stable microstructure with pore distribution. The porous structure enhances the substrate and oxygen diffusion rates required by cells. Increasing the PVA concentration affects the thickness or strength of the bead walls and reduces the number and size of macro pores.[68] However, this condition has been addressed by adding inorganic materials such as kaolin,[41] bentonite,[69] activated sludge,[70] and hectorite.

The influence of hectorite concentration, as shown in Fig. 10b shows that when the concentration is above 1%, the rate of MO degradation sharply decreases, ranging from 10% to 40%. High concentrations in the beads may have obstructed the cell space, adversely affecting bacterial activity.[41] The reported range of inorganic material concentrations supporting

Table 6 Kinetic equations for MO biodegradation

	BHec-RP			Free *R. pickettii*		
MO (mg L^{-1})	k (mg L^{-1} h^{-1})	$t_{1/2}$ (h)	R^2	k (mg L^{-1} h^{-1})	$t_{1/2}$ (h)	R^2
50	0.025	27.73	0.9034	0.015	46.21	0.9642
100	0.022	31.51	0.9384	0.014	49.51	0.9361
150	0.017	40.77	0.9754	0.007	99.02	0.9726
200	0.010	69.31	0.9471	0.003	231.05	0.9777
250	0.008	86.64	0.9525	0.003	231.05	0.9563
300	0.008	86.64	0.9561	0.003	231.05	0.9847

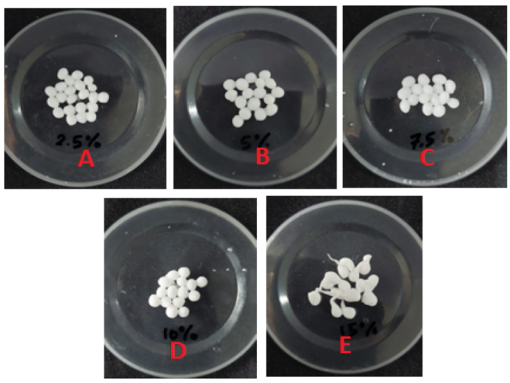

Fig. 11 Shape of beads at various PVA concentrations: (a) 2.5%; (b) 5%; (c) 7.5%; (d) 10%; (e) 15%.

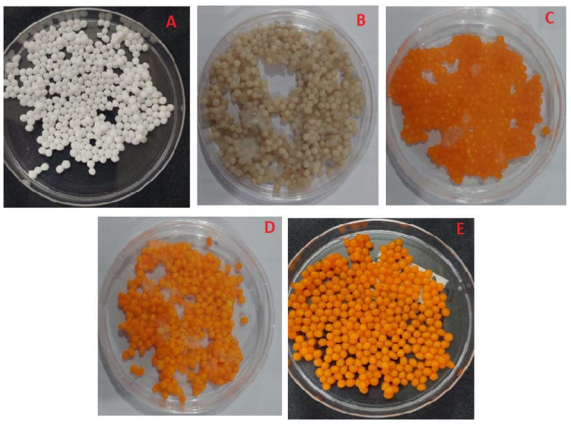

Fig. 12 Bead morphology: (a) before degradation (BHec-RP; live cells); (b) after degradation at pH 7 (BHec-RP; live cells); (c) after degradation at pH 5 (BHec-RP; live cells); (d) after degradation at pH 9 (BHec-RP; live cells); (e) after decolorization at pH 7 (BHec-RP; dead cells).

pollutant degradation efficiency in the immobilization systems is between 1% and 2.5%.[36,37,40,65] Generally, increasing the concentration of inorganic material in the immobilization matrix affects the mechanical properties of beads but has a negative influence on the ability of cells to degrade pollutants.[37,41,71,72] Based on the variations in PVA and hectorite concentrations, the optimal decolorization formulation consists of PVA 10% and hectorite 1%.

Effect of pH and temperature. Another crucial factor in MO degradation using immobilized cells is pH and temperature. In this research, the influence of the variable on the MO decolorization process is depicted in Fig. 10c and d. Fig. 10c shows the influence of pH ranging from 5 to 10, where the optimum degradation activity is achieved at pH 7 and a rate of 99%. The degradation rate significantly decreases under acidic and alkaline conditions, where there is competition between hydrogen ions and MO molecules for adsorption onto the surface of BHec-RP.[59,60] Meanwhile, alkaline conditions result in charge repulsion due to the increased negative charge of BHec-RP. The results showed that changes in the environmental degradation pH led to alterations in the cell and bead surface charges. Under acidic or alkaline conditions, the structure can be damaged, and enzymes may become inactive, showing no degradation activity.[73] The visualization of the pH influence on MO degradation rate is shown in Fig. 10c. The morphology of BHec-RP in Fig. 12a–d confirms that the MO decolorization process is highly dependent on pH changes. Fig. 12e is BHec-RP (dead cells) that only shows an adsorption process; hence, its bead morphology is the same as in Fig. 12c and d. This morphology shows that the MO decolorization process occurs due to degradation by *R. pickettii*.

Another factor influencing MO degradation by BHec-RP is temperature, as shown in Fig. 10d. These results show that the optimum temperature is achieved at 40 °C. Generally, the optimum biodegradation temperature range is around 30–40 °C,[12,74] showing that *R. pickettii* is a mesophilic bacterium, and higher optimum temperatures can be found in thermophilic bacteria.[75] At high temperatures, cell viability decreases, and enzymes included in MO degradation can denature.[76] For some bacteria, such as *Aeromonas hydrophila*, *Pseudomonas* sp, and *Shewanella oneidensis* MR-1, the optimum temperature is achieved in the range of 35–40 °C.[12,59,77]

Effect of reuse and residual viable cell. The repeated use of immobilized cells can reduce cell waste, save time, and lower cultivation costs,[78] and the reusability of BHec-RP is shown in Fig. 13. The results show stable degradation efficiency in cycles 1–3, with a decline observed in cycles 4–8. In the seventh and eighth cycles, BHec-RP starts to weaken and easily breaks due to over-swelling. The high degradation efficiency and stability of BHec-RP during the reusability test suggest that the immobilization methods are suitable for application in waste treatment. The stability of beads influences the reusability of MO decolorization by *R. pickettii*, as reported in other studies on *Bacillus fusiformis* (BFN), nitrifying bacteria,[40] and *Bacillus mycoides*.[41]

The decline in MO removal activity is consistent with the decrease in *R. pickettii* CFU counts. The reduction in immobilized cell numbers can be attributed to a combination of cell death, matrix leakage (if entrapped), diffusion pathway blockage, and waste toxicity.[79] Wojcieszynska *et al.*[80] reported that while this immobilization system offers several advantages, increasing the number of immobilized cell cycles leads to matrix pore blockage, limiting oxygen and nutrient diffusion.

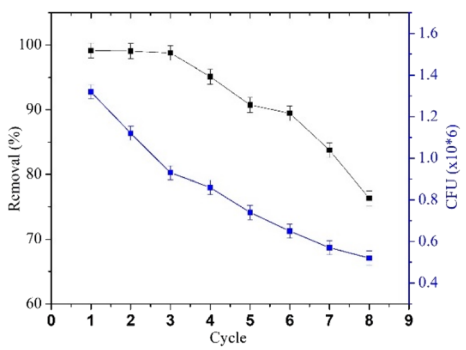

Fig. 13 MO degradation cycles and residual viable cell.

These conditions negatively impact the cells within the beads and their degradation efficiency. For instance, *R. pickettii* immobilized using an alginate–polyvinyl alcohol–bentonite matrix exhibited a significant decrease in OD600 and demonstrated degradation effectiveness for only two cycles.[81] In contrast, studies on immobilized bacterial-fungal consortium cells in a PVA matrix reported Direct Fast Scarlet 4BS degradation effectiveness for up to 30 cycles,[82] a consortium on *B. laterosporus*/*G. geotrichum* immobilized on coconut peat showed textile effluent degradation effectiveness (>80%) for up to 7 cycles.[83] These cases highlight that several other factors influence the performance of immobilized bacteria in pollutant degradation over multiple cycles. Cell type, consortium composition, matrix quality, and immobilization method appear to significantly impact cell stability.

Identification of enzymes and degradation metabolites

Enzymes found in the decolorization reaction are broadly categorized into two main groups, namely reducing and oxidizing. Lignin, peroxidase, laccase, tyrosinase, azoreductase, riboflavin reductase, NADH-DCIP reductase, and aminopyrine *N*-demethylase were reported to be included in the degradation of azodyes.[59,84,85] Srinivasan *et al.*[13] reported that enzymes produced by each bacterial species are responsible for the dye molecule's structure fragmentation. This research stated the activity of azoreductase and NADH-DCIP reductase, as reducing enzymes, and laccase, representing oxidizing enzymes, as summarized in Table 7.

To get insight into the MO decolorization mechanism by *R. pickettii*, the activities of azoreductase, NADH-DCIP reductase, and laccase were determined before (just after inoculation, *i.e.*, 0 h) and after decolorization (*i.e.*, within 48 h of incubation). The azoreductase assay was performed in a 2.0 mL reaction mixture containing 4.45 μM× methyl red, 0.2 mL enzyme solution, and 50 mM potassium phosphate buffer (pH 7.5). After the addition of 100 μM NADH to initiate the reaction, the reductive cleavage of methyl red was monitored spectrophotometrically at 430 nm (δ 430 nm = 23 360 M^{-1} cm^{-1}).[86] NADH–DCIP reductase activity was measured using a reaction mixture containing 25 μM DCIP and 0.2 mL of enzyme solution in 50 mM potassium phosphate buffer (pH 7.5). A 2.0 mL aliquot from the reaction mixture was combined with 250 μM NADH. The nicotinamide adenine dinucleotide-dichlorophenol indophenol (NADH-DCIP) reductase assay involved monitoring the reduction in color intensity of DCIP at a wavelength of 590 nm, which was monitored spectrophotometrically (ε = 19 mM^{-1} cm^{-1}).[87] Laccase enzyme activity was conducted through the observation of an increase in absorbance at 420 nm, which was attributed to the oxidation of the 2,2′-azino-bis(3-ethylbenzthiazoline)-6-sulfonate (ABTS) compound.[88] One unit of laccase activity is defined as the amount of enzyme required to oxidize 1 nmol of ABTS per minute at 28 °C.

Table 7 Enzyme activities in the decolorization of MO

Enzyme	Control	*R. pickettii* (free cell)	BHec-RP
Laccase[b]	1.2143	308.642	46.2963
Azo-reductase[b]	2.9474	124.857	26.0572
NADH-DCIP-reductase[a]	25.2217	221.053	37.0709
Laccase[b]	1.2143	308.642	46.2963

[a] μg of DCIP reduced min^{-1} mg^{-1} protein. [b] μmol min^{-1} mg^{-1} protein.

Table 7 shows that the extracellular crude enzyme activity in the control group is lower than in free *R. pickettii* and immobilized cells (BHec-RP). Similar results were reported in *Kocuria rosea* (MTCC 1532), showing an increase in laccase, azoreductase, and NADH-DCIP reductase activities after induction with MO and malachite green.[76,89] In this research, the activity of laccase, azoreductase, and NADH-DCIP reductase enzymes was higher than undere immobilization conditions. The significant difference in enzyme activity between free and immobilized cells is attributed to position. In free cells, secreted enzymes are suspended in the decolorization medium. In immobilized cells, a significant portion of enzymes is protected within the matrix, resulting in lower measured activity. The detection of extracellular enzyme activity shows that a part of the decolorization process occurs extracellularly. The three types of enzymes analyzed are most commonly reported in the decolorization of azo dyes.[49,51,75] The knowledge regarding the types of enzymes shows the character of the produced metabolites. For example, azoreductase is responsible for symmetric cleavage, while laccase and LiP function asymmetrically,[8] and NADH-DCIP reductase is included in reduction reactions.[90] These enzymes play a crucial role in breaking down the azo dyes, leading to the decolorization process.[75,91–93] The different functions of each enzyme provide insight into the specific mechanisms involved in the degradation of these compounds. Understanding the types of enzymes involved can also help in optimizing bioremediation processes for more efficient and effective dye removal from industrial wastewater.[94] Additionally, further research on the metabolites produced by these enzymes can provide valuable information for designing tailored enzyme cocktails for enhanced decolorization performance.

Identification of metabolites and proposed determination of biodegradation pathway

Identification of post-degradation dye metabolites is crucial to understanding the extent of pollutant degradation. The search for microbial strains with exceptional pollutant mineralization capabilities is the focus of different studies since microbial processes are categorized as environmentally safe green processes. However, the capabilities of microbial cells vary, specifically in the ability to produce enzymes that play a role in breaking down the molecular structure of pollutants. In this analysis, the identification of metabolites was performed using LC-QTOF-MS, as shown in Fig. 14. The chromatogram shows five different peaks compared to the control, predicted to be metabolites at retention times of 2.78, 2.98, 3.52, 4.65, and 5.97 minutes. Meanwhile, the control peak for MO is present at a retention time of 7.28 minutes.

Raw data from the LC-QTOF-MS analysis was processed using MZmine software version 2.53 to obtain specific spectra

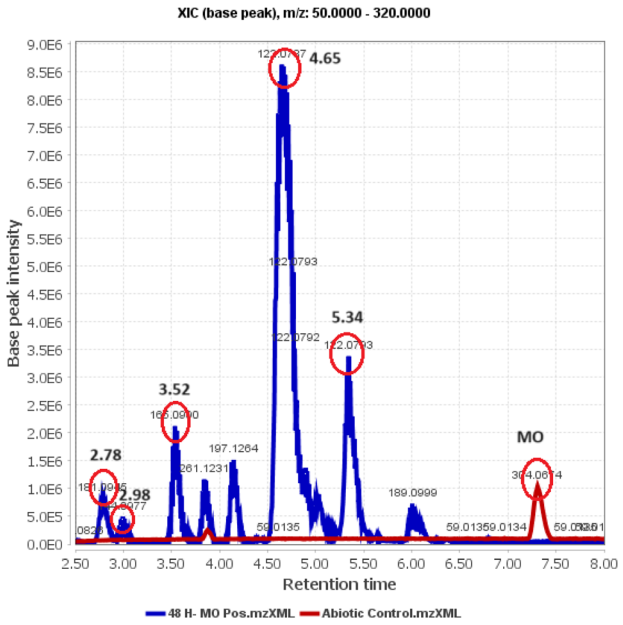

Fig. 14 Chromatogram of MO control (blue line) and degradation results.

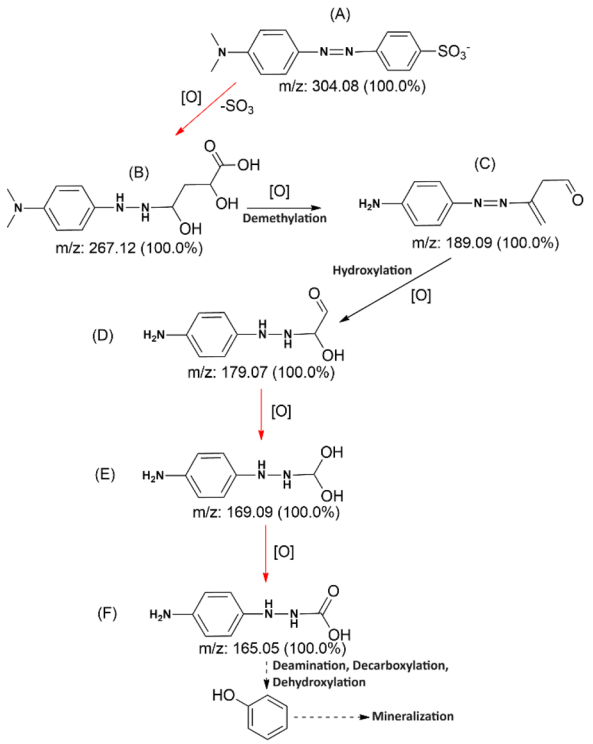

Fig. 15 Prediction of MO biodegradation pathway.

for the target peaks. Different chromatographic peaks at specific retention times are suspected to be metabolites resulting from the degradation of MO by immobilized *R. pickettii*. Based on the mass spectra, fragments of the suspected metabolites were obtained, as shown in Table 8. The molecular structure prediction of MO metabolites was based on reference methods and PathPred (**https://www.genome.jp/tools/pathpred/**).[8] This resulted in several predicted molecular fragmentations with successive *m*/*z* values following the sequence of symbols (B) 267.12; (C) 189.09; (D) 179.07; (E) 169.09; and (F) 165.05. Symbol A represents the basic structure of MO. This data shows that MO is subjected to fragmentation towards simpler molecules by opening the aromatic ring. Similar patterns have been observed in some bacteria applied for MO degradation and certain azo dyes, such as *Franconibacter* sp. 1 MS,[8] *Kocuria rosea* MTCC 1532 (ref. 89), and *Aeromonas hydrophila*.[59]

Fig. 15 shows the predicted biodegradation pathway of MO, where a desulfonation and aromatic structure oxidation reaction occurs from molecule A to B. Enzymatic reactions leading to the transformation of molecule B into an open-chain structure have been obtained using the Predicted Pathway application. The first reaction in this pathway includes desulfonation and hydroxylation on the aromatic ring, which dioxygenase enzymes can catalyze. Mono- and dioxygenase enzymes, phenol hydroxylase, and catechol-2,3-dioxygenase are commonly found in *R. pickettii*, catalyzing the oxidation of aromatic rings such as toluene. Meanwhile, hydroxylation is an enzymatic mechanism that facilitates the transformation of functional groups into carbonyl, acetyl, and decarboxylation. The proposed degradation sequence seems logical due to the similar patterns formed.[95]

Molecular fragmentation from B to F comprises complex reactions that may include various oxidoreductase and oxygenase enzymes, based on the PathPred application. However, the identified enzymes are azoreductase and NADH-DCIP reductase, which are included in the reduction of azo bonds.[75] These two enzymes show higher activity than the control, showing that MO and its fragments successfully induce the biosynthesis of reducing enzymes. These two enzymes show higher activity than the control, showing that MO and Its fragments successfully induce the biosynthesis of reducing enzymes. Overall, the degradation pathway of MO involves a series of intricate reactions mediated by specific enzymes.

Table 8 List of predicted structures of MO metabolites

RT	M/Z	Name	Molecular formula	Structure
2.78	267.12	4-(2-(4-(Dimethylamino)phenyl)hydrazinyl)-2,4-dihydroxybutanoic acid	$C_{12}H_{19}N_3O_4$	B
2.98	189.09	3-((4-Aminophenyl)diazenyl)but-3-enal	$C_{10}H_{11}N_3O$	C
3.52	179.07	2-(2-(4-Aminophenyl)hydrazinyl)-2-hydroxyacetaldehyde	$C_8H_{11}N_3O_2$	D
4.65	169.09	(2-(4-Aminophenyl)hydrazinyl)methanediol	$C_7H_{11}N_3O_2$	E
5.34	165.05	2-(4-Aminophenyl)hydrazinecarboxylic acid	$C_7H_9N_3O_2$	F

Through the reduction of azo bonds by enzymes such as azoreductase and NADH-DCIP reductase, MO and its fragments are successfully broken down into simpler molecules.[49,96] This process demonstrates the effectiveness of MO in inducing the biosynthesis of reducing enzymes, ultimately aiding in the breakdown of the compound into carbonyl, acetyl, and decarboxylation functional groups. The logical progression of molecular fragmentation seen in this study further supports the proposed degradation sequence for MO.

The fragmentation of MO varies significantly depending on the microbial strain used. Different strains will undoubtedly adopt their own pathways and enzymes. Several studies have shown that MO is subjected to both symmetric and asymmetric fragmentations, which are catalyzed by azoreductase and lignin peroxidase, respectively.[8,97] Furthermore, laccase is strongly included in thiazole yellow G's desulfonation and demethylation reactions.[98] This confirms that *R. pickettii* laccase is used in molecule A's desulfonation and demethylation reactions, resulting in the production of fragments B and C. Overall, the diverse enzymatic activities of different microbial strains play a crucial role in the fragmentation of MO. The involvement of azoreductase, lignin peroxidase, and laccase in these reactions highlights the complexity of the process.[26,75,99] The specific pathways and enzymes utilized by each strain further underscore the variability in MO fragmentation. These findings shed light on the intricate mechanisms involved in the degradation of MO by microbial communities.

Author contributions

Asranudin: conceptualization, methodology, investigation, validation, writing – original draft. Holilah: methodology, validation, supervision, writing – review & editing. Adi Setyo Purnomo: supervision, validation, writing – review & editing. Didik Prasetyoko: validation, supervision, writing – review & editing. Riki Subagyo: conceptualization, supervision. Noureddine El Messaoudi: validation, conceptualization. Alya Awinatul Rohmah: editing. Alvin Romadhoni Putra Hidayat: editing.

Conflicts of interest

There are no conflicts to declare.

Acknowledgements

The authors convey sincere thanks to Kemenristek-Dikti-Indonesia for their financial support through the Penelitian Disertasi Doktor (PDD) programme fund under contract number 1890/PKS/ITS/2023.

References

1 W. Song, J. Li, X. Zhang, J. Feng, X. Du, Q. Wang, C. Fu, W. Qiu, Z. Wang and X. Gao, *J. Environ. Manage.*, 2022, **308**, 114397.
2 Asranudin, A. S. Purnomo, D. Prasetyoko, H. Bahruji and Holilah, *Mater. Chem. Phys.*, 2022, **291**, 126749.
3 Asranudin, Holilah, A. S. Purnomo, H. Bahruji, D. Allouss, I. El Alaoui-elbalrhiti, R. Subagyo and A. Rohmah, *RSC Adv.*, 2022, **13**, 790–801.
4 Z. M. Şenol, N. El Messaoudi, Z. Ciğeroglu, Y. Miyah, H. Arslanoğlu, N. Bağlam, E. S. Kazan-Kaya, P. Kaur and J. Georgin, *Food Chem.*, 2024, **450**, 139398.
5 M. El Khomri, N. El Messaoudi, A. Dbik, S. Bentahar, Y. Fernine, A. Bouich, A. Lacherai and A. Jada, *Emergent Mater.*, 2022, **5**, 1679–1688.
6 Z. Cigeroglu, N. El Messaoudi, Z. M. Senol, G. Baskan, J. Georgin and S. Gubernat, *Mater. Today Sustain.*, 2024, **26**, 100735.
7 B. B. Hameed and Z. Z. Ismail, *Biochem. Eng. J.*, 2018, **137**, 71–77.
8 D. Baena-Baldiris, A. Montes-Robledo and R. Baldiris-Avila, *Omega*, 2020, **5**, 28146–188157.
9 R. El Kaim Billah, A. Zaghloul, H. A. Ahsaine, A. BaQais, I. Khadoudi, N. El Messaoudi, M. Agunaou, A. Soufiane and R. Jugade, *Int. J. Environ. Anal. Chem.*, 2022, 1–17.
10 F. Qu, K. Elomari, A. Wagner, A. De Simone and K. Beis, *Biochem. J.*, 2019, **476**, 3649–3660.
11 L. Ayed, E. Khelifi, H. Ben Jannet, H. Miladi, A. Cheref, S. Achour and A. Bakhrouf, *Chem. Eng. J.*, 2010, **165**, 200–208.
12 U. Roy, S. Sengupta, P. Banerjee, P. Das, A. Bhowal and S. Datta, *J. Environ. Manage.*, 2018, **223**, 185–195.
13 S. Srinivasan, K. P. M and S. Nagaraj, *Latest Innovations in Bacterial Degradation of Textile Azo Dyes*, INC, 2020.
14 H. Lade, S. Govindwar and D. Paul, *Int. J. Environ. Res. Public Health*, 2015, **12**, 6894–6918.
15 Y. Wang, L. Jiang, H. Shang, Q. Li and W. Zhou, *Environ. Technol. Innovation*, 2020, **19**, 100810.
16 K. O. Iwuozor, J. O. Ighalo, E. C. Emenike, L. A. Ogunfowora and C. A. Igwegbe, *Curr. Res. Green Sustainable Chem.*, 2021, **4**, 100179.
17 A. Haji and M. Naebe, *J. Cleaner Prod.*, 2020, **265**, 121866.
18 Y. Jin, Y. Wu, J. Cao and Y. Wu, *J. Taiwan Inst. Chem. Eng.*, 2014, **45**, 589–595.
19 N. El Messaoudi, Z. Ciğeroğlu, Z. M. Şenol, M. El Hajam and L. Noureen, *J. Water Process Eng.*, 2023, **55**, 104150.
20 N. El Messaoudi, Z. Ciğeroğlu, Z. M. Şenol, E. S. Kazan-Kaya, Y. Fernine, S. Gubernat and Z. Lopicic, *Biomass Convers. Biorefin.*, 2024, **2024**, 1–22.
21 S. Chowdhury, R. Mishra, P. Saha and P. Kushwaha, *Desalination*, 2011, **265**, 159–168.
22 Z. Irshad, I. Bibi, A. Ghafoor, F. Majid, S. Kamal, S. Ezzine, Z. M. Elqahtani, N. Alwadai, N. El Messaoudi and M. Iqbal, *Results Phys.*, 2022, **42**, 106006.
23 B. Saba, A. D. Christy, T. Park, Z. Yu, K. Li and O. H. Tuovinen, *Appl. Biochem. Biotechnol.*, 2018, **186**, 1017–1033.
24 T. R. Alkas, R. Ediati, T. Ersam, R. Nawfa and A. S. Purnomo, *Arabian J. Chem.*, 2022, **15**, 104129.
25 M. B. Kurade, T. R. Waghmode, J. Q. Xiong, S. P. Govindwar and B. H. Jeon, *J. Cleaner Prod.*, 2019, **213**, 884–891.
26 S. K. Sen, S. Raut, P. Bandyopadhyay and S. Raut, *Fungal Biol. Rev.*, 2016, **30**(3), 112–133.

27 M. Zhao, P. Sun, L. Du and G. Wang, *Environ. Sci. Pollut. Res.*, 2014, 6136–6145.
28 J. Cao, E. Sanganyado, W. Liu, W. Zhang and Y. Liu, *J. Environ. Manage.*, 2019, **242**, 229–237.
29 X. Zhang, H. Song, Y. Chen, M. Zhuang and W. Liu, *Int. Biodeterior. Biodegrad.*, 2021, **157**, 105142.
30 S. Srinivasan and S. K. Sadasivam, *J. Water Process Eng.*, 2018, **22**, 180–191.
31 S. C. D. Sharma, Q. Sun, J. Li, Y. Wang, F. Suanon, J. Yang and C. P. Yu, *Int. Biodeterior. Biodegrad.*, 2016, **112**, 88–97.
32 Y. Cheng, H. Y. Lin, Z. Chen, M. Megharaj and R. Naidu, *Ecotoxicol. Environ. Saf.*, 2012, **83**, 108–114.
33 M. N. Kathiravan, S. A. Praveen, G. H. Gim, G. H. Han and S. W. Kim, *Bioprocess Biosyst. Eng.*, 2014, **37**, 2149–2162.
34 T. R. Alkas, A. S. Purnomo, R. Ediati and T. Ersam, *RSC Adv.*, 2023, **13**, 30885–30897.
35 S. H. Liu, Z. T. Zeng, Q. Y. Niu, R. Xiao, G. M. Zeng, Y. Liu, M. Cheng, K. Hu, L. H. Jiang, X. F. Tan and J. J. Tao, *Sci. Total Environ.*, 2019, **655**, 1279–1287.
36 B. Ruan, P. Wu, M. Chen, X. Lai, L. Chen, L. Yu, B. Gong, C. Kang, Z. Dang, Z. Shi and Z. Liu, *Ecotoxicol. Environ. Saf.*, 2018, **162**, 103–111.
37 C. Lin, L. Gan, Z. Chen, M. Megharaj and R. Naidu, *Biochem. Eng. J.*, 2014, **90**, 1–7.
38 A. S. Purnomo, S. R. Putra, H. S. Putro, A. Hamzah, N. A. Rohma, A. A. Rohmah, H. D. Rizqi, Asranudin, B. V. Tangahu, I. D. A. A. Warmadewanthi and K. Shimizu, *RSC Adv.*, 2023, **13**, 21163–21170.
39 A. Dzionek, D. Wojcieszyńska and U. Guzik, *Electron. J. Biotechnol.*, 2016, **23**, 28–36.
40 Y. Zhang, Z. Yu, Y. Hu, C. Song, F. Li, W. He, X. Wang, Z. Li and H. Lin, *Environ. Technol. Innovation*, 2021, **22**, 101407.
41 H. Lin, Z. Chen, M. Megharaj and R. Naidu, *Appl. Clay Sci.*, 2013, **83–84**, 336–342.
42 R. R. Pawar, Lalhmunsiama, P. Gupta, S. Y. Sawant, B. Shahmoradi and S. M. Lee, *Int. J. Biol. Macromol.*, 2018, **114**, 1315–1324.
43 G. A. Płaza, J. Wypych, C. Berry and R. L. Brigmon, *World J. Microbiol. Biotechnol.*, 2007, **23**, 533–542.
44 A. S. Purnomo, D. Maulianawati and I. Kamei, *J. Microbiol. Biotechnol.*, 2019, **29**, 1424–1433.
45 A. S. Purnomo, A. Sariwati and I. Kamei, *Heliyon*, 2020, **6**, e04027.
46 P. A. Setyo, R. H. Dwi, F. Sri, P. H. Sulistyo and K. Ichiro, *Res. J. Chem. Environ.*, 2018, **22**, 151–156.
47 A. S. Purnomo, H. D. Rizqi, L. Harmelia, S. D. Anggraeni, R. E. Melati, Z. H. Damayanti and O. M. Shafwah, *Malays. J. Fundam. Appl. Sci.*, 2019, **15**, 377–380.
48 R. A. Hashem, R. Samir, T. M. Essam, A. E. Ali and M. A. Amin, *AMB Express*, 2018, 1–12.
49 M. M. Haque, M. A. Haque, M. K. Mosharaf and P. K. Marcus, *Saudi J. Biol. Sci.*, 2021, **28**, 793–804.
50 S. Barathi, C. Karthik and I. A. Padikasan, *Toxicol. Rep.*, 2020, **7**, 16–22.
51 I. Uribe-Arizmendi, M. A. Anducho-Reyes, M. R. Ramírez-Vargas, A. Cadena-Ramírez, C. R. Muro-Urista and A. Téllez-Jurado, *Water, Air, Soil Pollut.*, 2020, **231**(307), 1–14.
52 Lalhmunsiama, R. R. Pawar, S. M. Hong, K. J. Jin and S. M. Lee, *J. Mol. Liq.*, 2017, **240**, 497–503.
53 J. Zhang, C. H. Zhou, S. Petit and H. Zhang, *Appl. Clay Sci.*, 2019, **177**, 114–138.
54 I. Darah, M. Nisha and L. Sheh-Hong, *Appl. Biochem. Biotechnol.*, 2015, **175**, 2629–2636.
55 H. Ayama, P. Sumpavapol and S. Chanthachum, *Songklanakarin J. Sci. Technol.*, 2014, **36**, 291–299.
56 C. M. Earnest, *Thermochim. Acta*, 1983, **63**, 277–289.
57 A. M. Shanmugharaj, K. Yop and S. Hun, *J. Colloid Interface Sci.*, 2006, **298**, 854–859.
58 M. Asgari, A. Abouelmagd and U. Sundararaj, *Appl. Clay Sci.*, 2017, **146**, 439–448.
59 K. Velusamy, S. Periyasamy, P. S. Kumar, C. F. Caroline, T. Jayaraj, M. Gokulakrishnan and P. Keerthana, *Environ. Technol. Innovation*, 2022, **25**, 102126.
60 K. Akansha, D. Chakraborty and S. Ghosh, *Biocatal. Agric. Biotechnol.*, 2019, **18**, 101044.
61 D. Ş. Arslan, H. Ertap, Z. M. Şenol, N. El Messaoudi and V. Mehmeti, *J. Polym. Environ.*, 2024, **32**, 573–587.
62 A. R. P. Hidayat, D. O. Sulistiono, I. K. Murwani, B. F. Endrawati, H. Fansuri, L. L. Zulfa and R. Ediati, *J. Environ. Chem. Eng.*, 2021, **9**, 106675.
63 A. El Mouden, N. El Messaoudi, A. El Guerraf, A. Bouich, V. Mehmeti, A. Lacherai, A. Jada and J. H. Pinê Américo-Pinheiro, *Environ. Res.*, 2023, **225**, 115606.
64 Z. M. Şenol, E. Elma, N. El Messaoudi and V. Mehmeti, *J. Mol. Liq.*, 2023, **391**, 123310.
65 Y. Cheng, H. Lin, Z. Chen, M. Megharaj and R. Naidu, *Ecotoxicol. Environ. Saf.*, 2012, **83**, 108–114.
66 N. Khan, A. Ahmad, V. Sharma, A. K. Saha, A. Pandey and P. Chaturvedi Bhargava, *Renewable Energy*, 2022, **200**, 1589–1601.
67 M. H. El-Naas, A. I. Mourad and R. Surkatti, *Int. Biodeterior. Biodegrad.*, 2013, **85**, 413–420.
68 Z. Li-sheng, W. U. Wei-zhong and W. Jian-long, *J. Environ. Sci.*, 2007, **19**, 1293–1297.
69 B. Gong, P. Wu, Z. Huang, Y. Li, Z. Dang, B. Ruan, C. Kang and N. Zhu, *Chemosphere*, 2016, **148**, 388–394.
70 M. F. Bergero and G. I. Lucchesi, *J. Biotechnol.*, 2018, **272–273**, 1–6.
71 L. Yu, J. qiu Hua, H. cheng Fan, O. George and Y. Lu, *J. Hazard. Mater.*, 2020, **387**, 121697.
72 S. Mnasri Ghnimi and N. Frini-Srasra, *Appl. Clay Sci.*, 2018, **158**, 150–157.
73 G. Guo, X. Li, F. Tian, T. Liu, F. Yang, K. Ding, C. Liu, J. Chen and C. Wang, *Chemosphere*, 2020, **244**, 125510.
74 S. K. Garg and M. Tripathi, *Res. J. Microbiol.*, 2017, **12**, 1–19.
75 G. Guo, J. Hao, F. Tian, C. Liu, K. Ding, C. Zhang, F. Yang and J. Xu, *Bioresour. Technol.*, 2020, **316**, 123923.
76 G. Parshetti, S. Kalme, G. Saratale and S. Govindwar, *Acta Chim. Slov.*, 2015, **53**, 492–498.
77 P. Cai, X. Xiao, Y. He, W. Li, J. Chu and C. Wu, *Appl. Microbiol. Biotechnol.*, 2012, 1769–1776.
78 J. Y. Wu, S. C. J. Hwang, C. T. Chen and K. C. Chen, *Enzyme Microb. Technol.*, 2005, **37**, 102–112.

79 J. Liu, S. Li, X. Li, Y. Gao and W. Ling, *Environ. Technol.*, 2018, **39**, 2423–2433.
80 D. Wojcieszynska, A. Marchlewicz and U. Guzik, *Molecules*, 2020, **25**, 4473.
81 A. S. Purnomo, F. W. Hairunnisa, Misdar, V. P. Maria, A. A. Rohmah, S. R. Putra, H. S. Putro and H. D. Rizqi, *Heliyon*, 2024, **10**, e27871.
82 F. He, W. Hu and Y. Li, *Chemosphere*, 2004, **57**, 293–301.
83 M. B. Kurade, T. R. Waghmode, S. M. Patil, B. H. Jeon and S. P. Govindwar, *Chem. Eng. J.*, 2017, **307**, 1026–1036.
84 S. A. Misal and K. R. Gawai, *Bioresour. Bioprocess.*, 2018, **5**(17), 1–9.
85 R. L. Singh, P. K. Singh and R. P. Singh, *Int. Biodeterior. Biodegrad.*, 2015, **104**, 21–31.
86 G. D. Saratale, R. G. Saratale, J. S. Chang and S. P. Govindwar, *Int. Biodeterior. Biodegrad.*, 2011, **65**, 494–503.
87 H. S. Lade, T. R. Waghmode, A. A. Kadam and S. P. Govindwar, *Int. Biodeterior. Biodegrad.*, 2012, **72**, 94–107.
88 R. Al-Tohamy, S. S. Ali, R. Xie, M. Schagerl, M. A. Khalil and J. Sun, *Ecotoxicol. Environ. Saf.*, 2023, **263**, 115258.
89 G. K. Parshetti, A. A. Telke, D. C. Kalyani and S. P. Govindwar, *J. Hazard. Mater.*, 2010, **176**, 503–509.
90 L. N. Du, M. Zhao, G. Li, F. C. Xu, W. H. Chen and Y. H. Zhao, *Int. Biodeterior. Biodegrad.*, 2013, **78**, 108–116.
91 S. Barathi, K. N. Aruljothi, C. Karthik, I. Arulselvi and I. A. Padikasan, *Biotechnol. Rep.*, 2020, **28**, e00522.
92 M. Bilal, M. Asgher, R. Parra-Saldivar, H. Hu, W. Wang, X. Zhang and H. M. N. Iqbal, *Sci. Total Environ.*, 2017, **576**, 646–659.
93 M. M. Haque, M. N. Hossen, A. Rahman, J. Roy, M. R. Talukder, M. Ahmed, M. Ahiduzzaman and M. A. Haque, *Chemosphere*, 2024, **346**, 140568.
94 G. Guo, J. Hao, F. Tian, C. Liu, K. Ding, J. Xu, W. Zhou and Z. Guan, *Ecotoxicol. Environ. Saf.*, 2020, **204**, 111073.
95 M. P. Ryan, J. T. Pembroke and C. C. Adley, *J. Appl. Microbiol.*, 2007, **103**, 754–764.
96 J. Cong, X. Xie, Y. Liu, Y. Qin, J. Fan, Y. Fang, N. Liu, Q. Zhang, X. Song and W. Sand, *RSC Adv.*, 2022, **12**, 1968–1981.
97 A. S. Purnomo, Asranudin, N. Rachmawati, H. D. Rizqi, R. Nawfa and S. R. Putra, *HAYATI J. Biosci.*, 2022, **29**, 146–154.
98 P. O. Bankole, A. A. Adekunle and S. P. Govindwar, *Biotechnol. Rep.*, 2019, **23**, e00327.
99 H. Nadaroglu, G. Mosber, A. A. Gungor, G. Adıguzel and A. Adiguzel, *J. Water Process Eng.*, 2019, **31**, 100866.